Density functional theory characterization of the structures of H_3AsO_3 and H_3AsO_4 adsorption complexes on ferrihydrite

Nelson Y. Dzade[1, 2*] *and Nora H. de Leeuw*[1, 2*]

[1]School of Chemistry, Cardiff University, Main Building, Park Place, Cardiff CF10 1DF, UK

[2]Department of Earth Sciences, Utrecht University, Princetonplein 9, 3584 CC, Utrecht, The Netherlands

E-mail: DzadeNY@cardiff.ac.uk (N.Y.D); deLeeuwN@cardiff.ac.uk (N.H.dL)

Abstract

Reactions occurring at ferric oxyhydroxide surfaces play an important role in controlling arsenic bioavailability and mobility in natural aqueous systems. However, the mechanism by which arsenite and arsenate complexes with ferrihydrite (Fh) surfaces is not fully understood and although there is clear evidence for inner sphere complexation, the nature of the surface complexes is uncertain. In this work, we have used periodic density functional theory calculations to predict the relative energies, geometries and properties of arsenous acid (H_3AsO_3) and arsenic acid (H_3AsO_4), the most prevalent form of As(III) and As(V), respectively, adsorbed on Fh(110) surface at intermediate and high pH conditions. Bidentate binuclear (BB(Fe−O)) corner-sharing complexes are shown to be energetically favoured over monodentate mononuclear complexes (MM(Fe−O)) for both arsenic species. The inclusion of solvation effects by introducing water molecules explicitly near the adsorbing H_3AsO_3 and H_3AsO_4 species was found to increase their stability on the Fh surface. The adsorption process is shown to be characterized by hybridization between the interacting surface Fe-*d* states and the O and As *p*-states of the adsorbates. Vibrational frequency assignments of the As–O and O–H stretching modes of the adsorbed arsenic species are also presented.

Graphical abstract

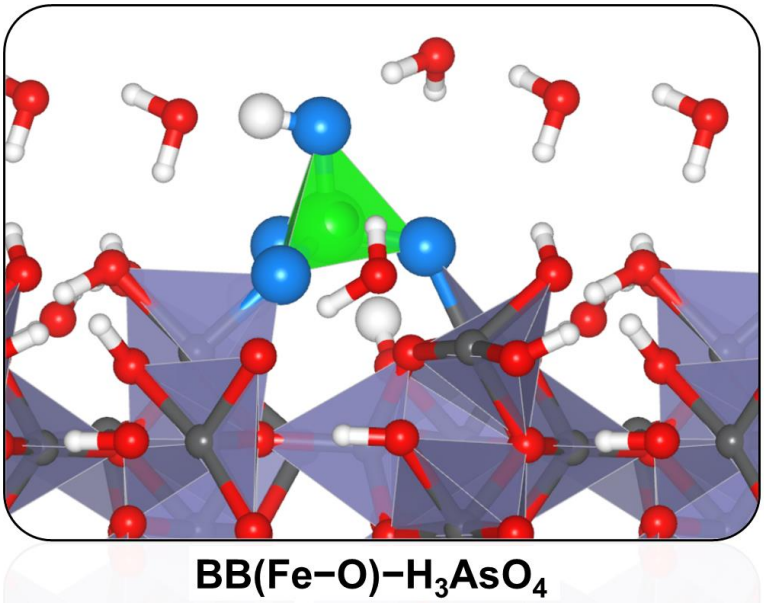

Environmental significance

The interfaces between iron oxides and aqueous solutions play a major role in the geochemistry of the Earth's surface environment by controlling the transport and fate of contaminants and pollutants, both natural and anthropogenic. An atomistic understanding of the adsorption mechanisms of arsenic species onto iron oxide surfaces is desirable for the development of efficient adsorptive media for the treatment of arsenic contaminated soils and surface waters. Our DFT calculations provide a molecular-level insight into the fundamental process of adsorption of arsenic on Fh(110) surface; predicting the registries of the adsorption complexes, adsorption energies, structural parameters, vibrational and electronic properties.

1. Introduction

Arsenic contamination of surface and ground waters represents a significant environmental hazard because of its high toxicity.[1,2] Natural processes, including soil erosion, mineral leaching, and weathering, are responsible for introducing arsenic into surface water.[3] Anthropogenic activities, particularly mineral extraction and processing, can also introduce arsenic-rich effluents into the environment if not carefully monitored and controlled.[4] Adsorption is a widely used technology for the removal of arsenic from solution.[5] Reactions

occurring at reactive iron oxide-hydroxides surfaces help control the sequestration, release, transport and transformation of arsenic-containing species in aqueous environments. It is well established that arsenic species form predominantly inner sphere complexes at hydrous iron oxide surfaces,[6–11] but the exact bonding geometries of arsenite and arsenate (mono- or bidentate) on the surfaces are still unknown.

Ferrihydrite (Fh) is a poorly crystalline and metastable ferric oxyhydroxide ($Fe_{10}O_{14}(OH)_2$), which is the main form of ferric iron in surficial environments. Because of its small size (ranging from 1–6 nm),[12,13] its abundance, and the geochemical reactivity of the constituent ferric ion, ferrihydrite plays an important role in iron cycling and in controlling the mobility and bioavailability of nutrient and toxic elements in the near-surface environment.[14–17] Lafferty and Loeppert (2005) compared the adsorption and desorption behaviour of As(V) and As(III) by ferrihydrite within the pH range from 3 to 11 and found that As(V) and As(III) strongly adsorb onto its surfaces.[18] The competitive adsorption of arsenate and arsenite with silicic acid at the ferrihydrite–water interface has been studied by Gao *et al*. over a wide pH range using experimental and modelling techniques.[19] Their extended X-ray absorption fine structure (EXAFS) analyses and DFT modeling suggested that arsenate tetrahedra are bonded to Fe metal centers *via* binuclear bidentate complexation with average As(V)−Fe bond distance of 3.27 Å.[19] Arsenite on the other hand was suggested to form both mononuclear bidentate and binuclear bidentate complexes at the ferrihydrite–water interface, as indicated by two As(III)–Fe bond distances of approximately 2.92–2.94 and 3.41–3.44 Å, respectively.[19] From EXAFS spectroscopy analysis, Waychunas *et al.* (1993) argued for bidentate complexes of arsenate at the ferrihydrite surface, resulting from corner-sharing between AsO_4 tetrahedra and edge-sharing pairs of FeO_6 octahedra.[9] Evidence of monodentate arsenate adsorption on ferrihydrite has been reported by Jain *et al.* (1999).[15]

Notwithstanding the extensive studies on surface complexation of arsenic at ferrihydrite, the fundamental adsorption mechanism, including the structures of the adsorption complexes, adsorption energies, and As−surface interatomic bond distances remain unresolved. The underlying physical driving forces that control the reactivity of the arsenic species with ferrihydrite surfaces also remain poorly understood, due to the diverse interactions and reactions occurring at the mineral−water interfaces. Such information cannot be obtained directly from EXAFS spectroscopy analysis, but molecular simulations offer an alternative route to providing mechanistic insights into the adsorption process and accurately determining the structures of arsenite and arsenate adsorption complexes onto iron oxide-hydroxide surfaces, which is critical for the quantification of the arsenic adsorption.[6,20–26] For example, Goffinet and Mason employed spin-polarized DFT calculations to study inner-sphere As(III) complexes on hydrated α-Fe_2O_3(0001) surface models.[20] Blanchard and co-workers have used DFT calculations to model the adsorption of arsenate on the hydrated $(1\bar{1}2)$ hematite surface, investigating charged inner- and outer-sphere complexes.[21] DFT modeling has also been employed to understand the adsorption reactions of arsenic on the surfaces of ferric hydroxides,[6,22] and iron sulfides.[27,28] However, to date, no systematic molecular-level investigation has been conducted to determine the relative energies, geometries and properties of arsenite and arsenate complexes on ferrihydrite surfaces, which makes this investigation timely.

To gain insight into the mechanisms of inner- and outer-sphere adsorption of H_3AsO_3 and H_3AsO_4 - the most common forms of As(III) and As(V), respectively at the Fh(110) surface under different pH different conditions, we have employed high quality periodic DFT calculations where electronic correlations are taken into account within the GGA +U approach. Our objective is to determine the energetic stability of different adsorption

configurations of H_3AsO_3 and H_3AsO_4 at Fh(110) surface under different pH conditions and extract the corresponding structural information (especially Fe−As and Fe−O interatomic distances). Insight into the electronic properties of the adsorbate-substrate systems is provided through analysis of projected density of states and differential charge density iso-surface contours. Vibrational frequency assignment of the As−O and O−H stretching modes for the different identified adsorption complexes of both arsenic species is also presented, which we consider will be useful for future experimental identification of the different adsorption complexes of As(III) and As(V) species at Fh–water interfaces.

2. Computational details

All geometry optimization calculations were implemented using the well-established VASP code,[29,30] which is based on the density functional theory (DFT). The interactions between the valence electrons and the cores were described with the projected augmented wave (PAW) method.[31] The electronic exchange-correlation potential was calculated using the GGA-PBE functional[32] with a Hubbard correction (PBE+U),[33] which accounts for the electron correlation in the localized *d*-Fe orbitals. The Hubbard correction approach has been shown to improve experimental agreement in calculated geometries, band structures and magnetic properties of Fe-containing compounds.[34–37] In this study, U_{eff} = 4 eV was found to provide an accurate description of the lattice parameters, interatomic distances and bond angles, in agreement with experiment. In our calculations each Fe is treated with 14 valence electrons with $3p^6d^7s^1$ projectors. Long-range dispersion forces were accounted for in our calculations using the Grimme DFT-D3 method,[38] which is essential for the accurate description of the interactions between the arsenic species and the ferrihydrite surface. A plane-wave basis set with a kinetic energy cut-off of 600 eV was tested to be sufficient to converge the total energy of the ferrihydrite to within 10^{-6} eV and the residual Hellman–Feynman forces on all

relaxed atoms reached 10^{-3} eV/Å. The Brillouin zone was sampled using 13 x 13 x 9 and 7 x 7 x 1 Monkhorst-Pack[39] K-points mesh for bulk and surface calculations, respectively, which ensures electronic and ionic convergence.

The ferrihydrite structure ($Fe_{10}O_{14}(OH)_2$) reported by Michel *et al.*[40], including H atoms whose initial positions were taken from the akdalaite structure,[41] was used as the starting point for the bulk ferrihydrite optimizations (**Figure 1**). Detailed descriptions of the structure and the optimized unit cell parameters are presented in Section 3.1. The Fh(110) surface, which is the most stable surface and one of the most commonly observed facets on ferrihydrite nanoparticles,[42] was created from the relaxed bulk material using the METADISE code,[43] which ensures the creation of surfaces with zero dipole moment perpendicular to the surface plane.[44] However, because of the adsorption of charged oxyanion species, in all surface calculations we have applied the Makov-Payne dipole correction perpendicular to the surface, as implemented in the VASP code,[45] to ensure that there is no net charge or monopole/dipole perpendicular to the surfaces, which might otherwise affect the adsorption energetics and structures. The corrections for the total energy are calculated as the energy difference between a monopole/dipole and quadrupole in the current supercell and the same dipole placed in a super cell with the corresponding lattice vector approaching infinity. The converged Fh(110) surface slab was constructed of eight iron layers, of which the five topmost layers were allowed to relax during optimization, while the bottom three layers were kept fixed in their bulk positions so as to represent a semi-infinite bulk crystal. Convergence of the surface energy of the Fh(110) slab with an increase in the number of topmost layers that are allowed to relax unconstrainedly is shown in the Supporting Information **Table S1**. A vacuum region of 15 Å along the c-axis was tested to be sufficient to avoid interactions between the surface slab and its periodic image.

Different coordination modes of adsorbed H_3AsO_3 and H_3AsO_4 species were examined, involving bidentate binuclear (BB) and monodentate mononuclear (MM) configurations, in order to obtain the most stable adsorption complexes. The adsorption energy (E_{ads}), which quantifies the strength of the adsorbate−surface interactions, was calculated as follows:

$$E_{ads} = E(\text{Fh+arsenic}) - [E(\text{Fh}) + E(\text{arsenic})] \quad (1)$$

where E(Fh+arsenic) represents the total energy of the ferrihydrite-arsenic complex, E(Fh) corresponds to the total energy of the appropriate hydrated Fh(110) surface, and E(arsenic) is the total energy of the free or solvated H_3AsO_3 or H_3AsO_4 molecules. The effect of solvation on the energies of aqueous and surface species was modelled by inclusion of four explicit water molecules near each adsorbate, including the initial surface functional groups. The total energies of the isolated or solvated H_3AsO_3 or H_3AsO_4 molecules, needed as reference energies, were calculated in a box of $15 \times 15 \times 15$ Å^3.

Insight into electron density redistribution within the Fh−adsorbate systems due to arsenic adsorption on the Fh(110) surface was gained from differential charge density ($\Delta\rho$) iso-surface plots, obtained as follows:

$$\Delta\rho = \rho(\text{Fh+arsenic}) - [\rho(\text{Fh}) + \rho(\text{arsenic})] \quad (2)$$

where ρ(Fh+arsenic), ρ(Fh) and ρ(arsenic) represent the electron density of the Fh-arsenic complex, the appropriately hydrated Fh(110) surface and the free H_3AsO_3 or H_3AsO_4 molecules, respectively. Vibrational frequency calculations were performed within the framework of the self-consistent density functional perturbation theory.[46] Vibrational modes were assigned by using the Jmol software to visualize the eigenvectors, which tells us how the atoms are displaced in the vibration.

3. Results and discussions

3. 1 Bulk structural properties

The crystalline ferrihydrite structure according to the Michel model[40] can be described adequately by a single-phase model, with the hexagonal space group *P63mc* and a unit cell with average dimensions of a = ~5.95 Å and c = ~9.06 Å (**Figure 1**). In its ideal formula of $Fe_{10}O_{14}(OH)_2$, the ferrihydrite structure consists of 20% FeO_4 (*i.e.* 20% tetrahedral Fe sites) and 80% FeO_6 (*i.e.* 80% octahedral Fe sites) polyhedra (**Figure 1a**). The Fe atoms are arranged in layers perpendicular to the crystallographic c-axis, occupying three symmetry-distinct sites, denoted as Fe1, Fe2, and Fe3, as shown in **Figure 1b**. The Fe1 sites comprise edge-sharing Fe-octahedra forming layers consisting exclusively of Fe1. These layers are separated by a mixed layer of octahedrally coordinated Fe2 sites (which occupy a different Wyckoff symmetry position and have slightly different Fe−O bonding geometries than the Fe1 octahedra) and tetrahedrally coordinated Fe3 sites.

Using the theoretical methods described above and allowing all atoms to fully relax until the required accuracy was reached, we calculated the unit cell parameters at a = 5.955 Å and c = 9.222 Å (**Table 1**), which compares well with an earlier theoretical prediction (a = 5.97Å and c = 9.37 Å),[47] and experimental values reported by Michel *et al.*[40] (**Table 1**). Our calculated tetrahedral and octahedral Fe−O bond distances also show good agreement with experiment and earlier theoretical predictions.[47,48] The fully relaxed ferrihydrite structure obtained shows an approximately symmetrical tetrahedral Fe3−O bonding arrangement, with four Fe−O bonds of nearly equivalent length (1.903 Å x 1, 1. 913 Å x 3) consistent with tetrahedral Fe^{3+}. The experimental tetrahedral Fe−O bond distance along the c-axis of the structure is only 1.790 Å, while the other three Fe−O bonds in the tetrahedron are 1.952 Å in length.[48] The octahedral Fe1−O and Fe2−O bond distances are calculated respectively at

1.968 Å x 2; 2.059 Å x 2; 2.029 Å; and 2.066 Å; 1.942 Å x 3; and 2.183 Å x 3. The O−H bond distance in the ferrihydrite structure converged at 0.985 Å, similar to the 1.000 Å obtained from a previous theoretical study.[47]

The arrangement of the oxygen anions and the high-spin iron cations in ferrihydrite naturally affects the orientation of the spin magnetic moment of the iron ions. In this study, we have probed different magnetic configurations and found that the lowest energy (ground) state corresponds to the ferrimagnetic structure (**Figure 1b**), in agreement with earlier theoretical predictions,[47] and experimental observations.[49] The ferrimagnetic structure corresponds to a layered structure in which planes of Fe moments alternate in alignment along the c-axis.[47, 49] The magnetic moment for the octahedral Fe1 and Fe2 are calculated at 4.20 μB and 4.17 μB, whereas the tetrahedral Fe3 has a magnetic moment of 4.13 μB.

3.2 Surface model and adsorption conditions

The Fh(110) surface slab was constructed of eight layers of iron and contains a total of 112 atoms (Fe = 40, O = 64, and H = 8). The Fh(110) surface has two possible terminations (term-A and term-B) as shown in the Supporting Information, **Figure S1**, both of which were considered in order to determine the most stable termination. To quantify the structural stabilities of the two terminations of the Fh(110) surfaces, we have calculated their surface energies (γ_r), defined as:

$$\gamma_r = \frac{E_{slab}^{relaxed} - nE_{bulk}}{2A} \tag{3}$$

where $E_{slab}^{relaxed}$ is the energy of the relaxed slab, nE_{bulk} is the energy of an equal number (n) of bulk Fh units, and A is the area of one side of the slab. Under dehydrated and hydrated conditions, Term-A of the Fh(110) surface is found to be thermodynamically more stable

than term-B, thus Fh(110)-term-A was employed for the subsequent characterization of arsenic complexation. The surface energies of the dehydrated and hydrated Fh(110)-term-A surface are calculated at 0.88 and 0.67 Jm^{-2}, whereas those for Term-B are calculated at 1.24 and 0.98 Jm^{-2}, respectively. As is to be expected, hydration of both terminations is found to have a stabilizing effect, since the adsorption acts to coordinate the water molecules to the under-coordinated Fe ions, thus providing a closer match to bulk coordination of the surface species.

The most stable term-A has four octahedral Fe ions (Fe_{oct}) in the topmost layer, two of which are in three-fold coordination with oxygen, whereas the other two are in four-fold coordination with oxygen. The reduction in the coordination number from six, as is found in the bulk, can be attributed to the breaking of bonds to create the surface. The tetrahedral Fe_{tet} ions are in the second layer of the slab, as shown in blue colour (**Figure 2 & 3**). When the most stable Fh(110)-term-A surface is hydrated by adsorbing four water molecules at each topmost Fe_{oct} ion site, two of the water molecules adsorb molecularly at the four-fold Fe_{oct} sites, whereas the other two spontaneously dissociate upon adsorption at the three-fold Fe_{oct} sites, resulting in the formation of an Fh(110) surface with mixed -OH/-H_2O composition (**Figure 2**). The major interactions between the adsorbing water molecules and the Fh(110)-term-A surface occur through oxygen and the Fe_{oct} ions. The average Fe−O between the O atoms of the molecular and dissociated water molecules and the interacting Fe_{oct} ions was calculated at 2.102 Å and 1.878 Å, respectively. pH-dependent Fh(110) surfaces were considered by changing the number of H^+ on the surface, i.e. by adjusting the ratio of surface -OH/-H_2O functional groups on the Fh(110) surface, as has been suggested in the literature (see **Figure 4**).[50, 51] Under high pH conditions, there will be more H^+ on the surface; hence we expect all the water molecules to be dissociatively adsorbed (−OH covered surface), as shown

in **Figure 3**. The average Fe−OH bond distance was calculated at1.912 Å, whereas the newly formed O−H bonds converge at 1.03 Å.

After hydration and hydroxylation of the Fh(110) surface, the topmost Fe_{oct} ions become four- and five-fold coordinated by oxygen, although they are still under-coordinated compared to the bulk. These sites are hence expected to be reactive toward adsorbing As(III) and As(V) species. In aerobic waters, As(V) is predominately present as H_3AsO_4 at extremely low pH (< 2) (pK_{a1}= 2.19, pK_{a2}= 6.94, and pK_{a3}= 11.5); within a pH range of 2 to 11, it is replaced by $H_2AsO_4^-$ and $HAsO_4^{2-}$. For As(III), H_3AsO_3 appears at low pH and under mildly reduced conditions (pK_{a1}= 9.20), but it is replaced by $H_2AsO_3^-$ as the pH increases. Only when the pH exceeds 12 does $HAsO_3^{2-}$ appear. In this study, we have used H_3AsO_3 and H_3AsO_4 to characterize the reactivity of As(III) and As(V) with the Fh(110) surface covered with either mixed −OH/−H_2O composition (intermediate pH) or solely −OH composition (high pH). For As(V), we have also investigated the interactions of $H_2AsO_4^-$ as that is the dominant species in the experimental pH range from 4−9.

3.4 Surface adsorption complexes of H_3AsO_3

Arsenic species have been found to form predominantly inner sphere complexes at hydrous iron oxide surfaces.[6−11] In order to predict the lowest-energy adsorption complexes of H_3AsO_3 on the Fh(110) surface at intermediate and high pH conditions, different possible inner- and outer-sphere adsorption modes were examined. Specifically, three coordination modes have been evaluated: bidentate binuclear (BB), bidentate mononuclear (BM), and monodentate mononuclear (MM). However, the BM coordination converts to MM coordination during energy minimization. The optimized geometries of the H_3AsO_3 with and without solvation by four H_2O molecules at the mixed -OH/-H_2O covered Fh(110) surface are shown in **Figure 5**. The calculated adsorption energies and interatomic bond distances are summarized in **Table**

2. The most stable adsorption geometry of H_3AsO_3 at the mixed -OH/-H_2O covered Fh(110) surface was calculated to be a bidentate binuclear complex, BB(Fe−O), with and without solvation as shown in **Figure 5 (a** & **c**). In the BB(Fe−O) complexes, the H_3AsO_3 species interacts with the surface through two Fe−O bonds which are calculated at 2.091 Å and 1.950 Å for the solvated complexes, whereas for the non-solvated complexes they are 2.154 Å and 1.981 Å, as displayed in **Figure 5**. The adsorption energies for the BB complexes were calculated at −3.60 eV with solvation and −2.53 eV without solvation. The monodentate mononuclear (MM) complexes (**Figure 5(b & d**), wherein the H_3AsO_3 species interacts with the Fh surface through a single Fe−O bonds released an adsorption of −2.49 eV with solvation and −1.25 eV without solvation. The single Fe−O bonds with and without solvation were calculated at 1.951 Å and 2.104 Å, respectively. When H_3AsO_3 is adsorbed in an outer-sphere configuration (**Figure 5e**), a smaller adsorption energy of 1.25 eV is released compared to the solvated inner-sphere BB and MM complexes, which released adsorption energies of 3.60 eV and 2.49 eV, respectively. In the outer-sphere complex, H_3AsO_3 is stabilized on the surfaces through hydrogen-bonded interactions as displayed on **Figure 5e**. The large energy difference between the outer- and inner-sphere complexes suggests that H_3AsO_3 will preferentially form inner-sphere complexes on the Fh surface, in agreement with experimental observations.[9, 19] As is evident from the calculated large adsorption energies, the inclusion of solvation effects through the introduction of four explicit water molecules near each adsorbate was found to increase the stability of the H_3AsO_3 species on the Fh surface. The shorter Fe−O bonds calculated for the solvated H_3AsO_3 complexes compared to the non-solvated complexes is consistent with the stronger adsorption obtained with the inclusion of solvation effects. In both inner-sphere BB and MM complexes, we observe a single deprotonation of H to form a surface hydroxyl species (O−H 1.011 Å), suggesting that As(III) exist as $H_2AsO_3^-$ on the mixed −OH/−H_2O covered Fh(110) surface. We also observe

hydrogen-bonded interactions between the O ions of the H_3AsO_3 and the hydrogen of the solution water molecules (reflected in the short O−H distances in **Figure 5**), which we believe contributed to the stability of H_3AsO_3 on the surface. Due to the formation of strong Fe−O bonds, we observed elongations of the As−O bonds in the BB and MM adsorption complexes (**Table 2**), which is confirmed via vibrational frequency analysis, presented in Section 3.7. The strong Fe−O bonds arise from strong hybridization between the interacting Fe *d*-states and O p-states, which are characterized by electron redistribution within the bonding regions (see Supporting Information **Figure S3**).

At the -OH covered Fh(110) surface (*i.e.*, more H^+ on the surface), the optimized adsorption complexes of H_3AsO_3 displayed in **Figure 6** reveal that the bidentate binuclear (BB(Fe−O)) configuration is thermodynamically the most stable complex, with an adsorption energy of −3.39 eV compared to −2.23 for the MM(Fe−O) complex and −1.83 eV for the outer-sphere complex. The smaller adsorption energies calculated at the -OH covered Fh(110) surface compared to the mixed -OH/-H_2O covered surface, suggest that increasing the H^+ on the Fh surfaces has a destabilizing effect on the adsorption of H_3AsO_3. The two interacting Fe−O bonds in the BB(Fe−O) complex are calculated at 2.142 Å and 2.151 Å, whereas the single Fe−O bond in the MM(Fe−O) complex is calculated at 2.278 Å, as displayed in **Figure 6**. Hydrogen-bonded interactions (displayed in **Figure 6**) contribute to the stability of both the inner- and outer-sphere H_3AsO_3 adsorption complexes on the −OH covered Fh(110) surface.

3.5 Surface adsorption complexes of H_3AsO_4 and $H_2AsO_4^-$

As with H_3AsO_3, we have considered different possible inner and outer sphere adsorption geometries for H_3AsO_4 on the Fh(110) surface at intermediate pH (mixed -OH/-H_2O composition) and high pH (-OH composition, *i.e.*, more H^+ on the surface) conditions, in order to determine the lowest-energy adsorption structures. The optimized geometries of the

most stable inner-sphere bidentate binuclear (BB), monodentate mononuclear (MM) and outer-sphere complexes of H_3AsO_4 at the mixed -OH/-H_2O covered Fh(110) surface are shown in shown in **Figure 7**, whereas the calculated adsorption energies and optimized structural parameters are reported in **Table 3**. The formation of bidentate binuclear (BB(Fe−O)) complexes is found to be energetically favoured over monodentate mononuclear (MM(Fe−O)) complexes. The BB(Fe−O) complexes of H_3AsO_4 released an adsorption of 4.18 eV with solvation (**Figure 7c**) and 2.85 eV without solvation (**Figure 7a**. The two interacting Fe−O bonds for the solvated complex were calculated at 1.965 Å and 2.003 Å, whereas the non-solvated bonds are calculated at 2.010 Å and 2.077 Å, as displayed in **Figure 7**. Compared to the BB(Fe−O) complexes, the monodentate mononuclear MM(Fe−O) complexes released an adsorption energy of 2.84 eV with solvation (**Figure 7b**) and 1.34 eV without solvation (**Figure 7d)**. In the solvated MM(Fe−O) complex, the Fe−O bond distance is calculated at 1.987 Å, compared to 2.147 Å without solvation. The shorter Fe−O bonds calculated for the solvated complexes, compared to the non-solvated complexes, is consistent with the stronger adsorption calculated for the solvated complexes. Similar inner-sphere adsorption complexes were obtained for $H_2AsO_4^-$, although with slightly smaller adsorption energies compared to H_3AsO_4, as shown in **Table 3** and the Supporting Information **Figure S2**. The weaker adsorption of $H_2AsO_4^-$ can be attributed to the absence of one hydrogen-bonded interaction with the surface or to the absence of surface OH bond formation resulting from deprotonation. Hybridization between the interacting Fe *d*-states and O *p*-states to form the strong Fe−O bonds is shown to be characterized by electron redistribution within the bonding regions (see Supporting Information **Figure S4**).

When adsorbed in an outer-sphere complex, H_3AsO_4 is stabilized on the surfaces through hydrogen-bonded interactions, as displayed in **Figure 7e**, releasing a lesser adsorption energy

of 2.13 eV compared to the inner-sphere complexes **(Table 3)**. Whereas no deprotonation occurs in the outer-sphere complex, we observed that in the inner-sphere complexes a single deprotonation of H_3AsO_4 occurs to form an $H_2AsO_4^-$ derivative and a surface hydroxyl species (average O−H ~1.005 Å). The deprotonation of the inner-sphere complexes can be attributed to the strong Fe−O interactions, which resulted in the weakening of the O−H bond and hence their subsequent deprotonation onto the surface. Besides the shorter Fe−O bonds in the solvated inner-sphere complexes, we also observed that hydrogen-bonded interactions contribute to the increased stability of H_3AsO_4 on the surface, as displayed in **Figure 7**. In addition to elongations of the As−O bonds, we observed O−H bond stretches especially in the solvated complex (0.978−1.084 Å), which can be attributed to the presence of hydrogen-bonded interactions between the hydrogen atom of H_3AsO_4 and the O of the surface (O_{surf}) or water molecules (O_{wat}), as displayed in **Figure 7**.

At the -OH covered Fh(110) surface, an initial bidentate binuclear (BB(Fe−O)) configuration of H_3AsO_4 converts during energy minimization to a MM(Fe−O)-1 complex (**Figure 8a**), with single deprotonation to form $H_2AsO_4^-$ at the surface and a surface hydroxyl species (O−H =1.012 Å). This complex released an adsorption energy of 2.87 eV, compared to 2.54 eV for a similar MM(Fe−O)-2 complex without deprotonation (**Figure 8b**). The interacting Fe−O bonds are calculated at 1.958 Å for the deprotonated complex and 2.048 Å for the protonated complex. The outer-sphere complex, wherein the H_3AsO_4 is stabilized on the surface through hydrogen-bonded interactions, released an adsorption energy of 2.08 eV.

3.6 As−Fe interatomic distances: Calculated verses EXAFS data

Consistent with the findings in the present study, previous EXAFS studies of arsenic uptake on goethite and ferrihydrite indicate the prevalence of bidentate binuclear binding rather than monodentate binding of As(III) and As(V) onto the surfaces of these oxides.[7−11,19]

Monodentate complexes are considered to form only at very low surface sorption densities.[10, 11,52,53] Ona-Nguema *et al.* found, using EXAFS spectroscopy, that As(III) forms bidentate mononuclear edge-sharing and bidentate binuclear corner-sharing complexes on ferrihydrite.[7] Waychunas *et al.* stated that bidentate site attachment should be strongly favoured, both thermodynamically and kinetically, over monodentate attachment for As(III).[9,11] In the present DFT study, the As−Fe interatomic distances for the interaction of H_3AsO_3 at the Fh(110) interface were calculated at 3.616 Å and 3.185 Å for the MM(Fe−O) complex, with and without solvation, respectively. For the BB(Fe−O) complexes, As−Fe interatomic distances were calculated at 3.573 Å and 3.606 Å with and without solvation, respectively. In close agreement with our results, EXAFS data suggest As−Fe interatomic distances in the range of 2.92–3.44 Å, for arsenite−Fh interraction.[19] For the H_3AsO_4 adsorption complexes in the present study, the As−Fe interatomic distances were calculated at 3.268 Å and 3.402 Å for the MM(Fe−O) complex, with and without solvation, respectively, whereas in the BB(Fe−O) complexes, the As−Fe interatomic distances were calculated at 3.312 Å and 3.142 Å with and without solvation, respectively. EXAFS data showed that an As–Fe distance of 3.21–3.25 Å dominates arsenate–sorbed ferrihydrite.[19,54] Fendorf *et al.* used EXAFS to investigate As(V) adsorption on goethite (α−FeOOH) surfaces and, based on the different atomic distances measured, three complexes were postulated: a monodentate mononuclear complex (As−Fe = 3.6 Å), a bidentate binuclear complex (As−Fe = 3.24–3.26 Å), and a bidentate mononuclear complex (As−Fe = 2.83–2.85 Å).[53] We did not, however, observe any bidentate mononuclear complexes of H_3AsO_4 at the Fh(110) surface.

3.7. Vibrational properties

In order to determine the stability of the different adsorption complexes and provide an assignment for the As−O and O−H stretching modes of the adsorbed species, we have

computed the wavenumbers of the normal modes for the different adsorption configurations of H_3AsO_3 and H_3AsO_4 on the Fh(110) with mixed -OH/-H_2O composition (**Table 4**). No imaginary modes were observed for either arsenic species in any of the different adsorption complexes calculated, which suggests that the reported adsorption structures are all stable. Higher vibrational frequencies were calculated for the deprotonated As−O bonds compared to protonated As−O_H bonds, which is consistent with the shorter distances calculated for the deprotonated As−O bonds compared to the longer ones for the protonated As−O_H bonds. Similar results were obtained from Raman spectroscopy by Müller *et al*. for As(III) and As(V) in aqueous solutions and adsorbed on iron oxy-hydroxides. Their results indicate that the As−OH vibrations occur at lower wavenumbers than the uncomplexed As−O vibrations, which indicates that As−O bonds are shorter and stronger than As−OH.[56] For H_3AsO_3, the three As−O stretching modes were calculated at 622, 570, and 526 cm^{-1} for the non-solvated MM−(Fe−O) complex compared to 725, 616, and 559 cm^{-1} for the solvated MM−(Fe−O) complex. For the BB−(Fe−O) complexes, the solvated As−O stretching modes were calculated at 771, 665, and 448 cm^{-1}, whereas the non-solvated ones were obtained at 772, 683, and 482 cm^{-1} (**Table 4**). Our assigned As−O stretching vibrational modes of the adsorbed H_3AsO_3 species compare closely with those from an experimental work by Loehr *et al*.,[55] who reported 710, 655, and 655 cm^{-1} for arsenious acid in aqueous solution.

For the H_3AsO_4 species, higher frequencies were calculated for the deprotonated As−O stretching modes compared to the protonated As−O_H modes, in agreement with the shorter distances calculated for the deprotonated (As−O) bond than the protonated (As−O_H) bonds. Frequencies within the range of 800−940 cm^{-1} can be assigned to the free or deprotonated As−O bonds, whereas those in the range of 600−760 can be assigned to the protonated As−O_H bonds. Loehr *et al*. reported the As−O stretching mode at 790 cm^{-1} and the As−O_H stretching modes at 610 and 570 cm^{-1} for $H_2AsO_4^-$ species.[55] Similar assignments were

reported by Goldberg *et al*.[8] Higher frequencies within the range of 2000−3800 cm^{-1} can be assigned to the O−H stretching modes, which are similar to the O–H stretching modes of a water molecule.[57]

4. Summary and conclusions

In summary, we have performed a detailed atomic-level analysis of the structural geometries, vibrational and electronic properties of the adsorption complexes of H_3AsO_3 and H_3AsO_4 on Fh(110) surface at intermediate and high pH conditions, using periodic density functional theory calculations with dispersion correction. In agreement with EXAFS studies, our simulations show that bidentate binuclear complexes of both H_3AsO_3 and H_3AsO_4 are thermodynamically more favourable than monodentate mononuclear complexes at the Fh (110) surface. The relatively large adsorption energies calculated for the deprotonated complexes can be attributed to a number of factors. First, breaking a very weak O–H bond from either H_3AsO_3 or H_3AsO_4 species requires less energy than the energy released in the formation of the stronger OH bonds with surface oxygen. Second, the lower coordination of the surface-terminating Fe_{oct} ions contribute to their stronger reactivity towards the adsorbing H_3AsO_3 or H_3AsO_4 species, as reflected in the short Fe−O bonds calculated. Third, the enhancement in adsorption energy upon solvation can be attributed to the formation of hydrogen-bonded interactions between the complex and water molecules in solution or on the surface. However, our calculated adsorption energies are comparable with those calculated for arsenate at other iron oxyhydroxide (FeOOH) goethite (101), akaganeite (100), and lepidocrocite (010) surfaces.[22] On goethite (101) the adsorption energies for arsenate vary from E_{ads} = −0.97 eV to −4.21 eV. On akaganeite (100), the adsorption of a monodentate binuclear (mb) protonated arsenate complex was reported at −4.16 eV. On lepidocrocite (010), the monodentate binuclear complex with protonation was reported to have an

adsorption energy of E_{ads} = −3.57 eV. The calculated electronic structures highlight the importance of the hybridization between interacting surface Fe *d*-states and the adsorbates O and As *p*-states in determining the strength of the adsorbate−adsorbent interactions. We consider that the unique information, and specifically the distinction of the binding modes of H_3AsO_3 and H_3AsO_4 at the Fh(110) surface, as well as the deconvolution of the vibrational frequencies associated with the adsorption complexes, will provide useful guidance for future experimental investigations of As(III) and As(V) adsorption at the ferrihydrite–water interface, which should be transferable to other iron oxide minerals. Future investigations will expand the work presented here to include classical MD simulations which will provide a complete description of the dynamical processes occurring at the As−water−Fh(110) interfaces. The calculated adsorption structural parameters and energetics from this work will be useful in the derivation of force fields to be employed in the classical MD simulations to simulate more complex systems, including the adsorption of single and multiple As(III) and As(V) species adsorption from an explicit 3-dimensional aqueous environment.

Conflicts of interest

There are no conflicts to declare.

Acknowledgements

We acknowledge the Netherlands Organisation for Scientific Research (NWO) for funding (Grant No. 13CO26-2). This work was performed using the computational facilities of the Advanced Research Computing @ Cardiff (ARCCA) Division, Cardiff University. This work also made use of the facilities of ARCHER (http://www.archer.ac.uk), the UK's national supercomputing service via our membership of the UK's HEC Materials Chemistry Consortium, which is funded by EPSRC (EP/L000202).

References

1. P. Xu, G. M. Zeng, D. L. Huang, C. L. Feng, S. Hu, M.H. Zhao, C. Lai, Z. Wei, C. Huang, G. X. Xie, Z. F. Liu, *Science of the Total Environ.* 2012, **424**, 1–10.

2. H. P. Viet, H. T. Con, T. C. Ha, V. H. Ha, M. Berg, W. Giger, and R. Schertenleib, In Arsenic Exposure and Health Effects V, (W. R. Chappell, C. O. Abernathy, R. L. Calderon, and D. J. Thomas, Eds.), Amsterdam: Elsevier B.V., 2003, 459–469.

3. A. H. Welch, D. B. Westjohn, D. R. Helsel and R. B. Wanty, *Ground Water,* 2000, ***38,*** 589−604.

4. D. K. Nordstrom, *Science*, 2000, **296**, 2143−2144.

5. N. R. Nicomel, K. Leus, K. Folens, P. Van Der Voort, G. Du Laing, Int. *J. Environ. Res. Public Health* 2016, **13**, 62.

6. J. Farrell, J. B. K. Chaudhary, *Environ. Sci. Technol*. 2013, **47**, 8342−8347

7. G. Ona-Nguema, G. Morin, F. Juillot, G. Calas, G. E. Brown Jr., *Environ. Sci. Technol.*, 2005, **39**, 9147–9155.

8. S. Goldberg, C. T. Johnston, *J. Colloid Interface Sci.* 2001, **234**, 204–216.

9. G. A. Waychunas, B. A. Rea, C. C. Fuller, J. A. Davis, *Geochim. Cosmochim. Acta* 1993, **57**, 2251–2269.

10. B. A. Manning, S. E. Fendorf, S. Goldberg, *Environ. Sci. Technol.* 1998, **32**, 2383–2388.

11. G. A. Waychunas, J. A. Davis, C. C. Fuller, *Geochim. Cosmochim. Acta* 1995, **59**, 3655–3661.

12. R. A. Eggleton, R. A. Fitzpatrick, *Clays and Clay Minerals*, 1988, **36**, 111–124.

13. D. E. Janney, J. M. Cowley, P. R. Buseck, *Clays and Clay Minerals*, 2000, **48**, 111–119.

14. K. P. Raven, A. Jain, R. H. Loeppert, *Environ. Sci. Technol.* 1998, **32**, 344−349.

15. A. Jain, K. P. Raven, R. H. Loeppert, *Environ. Sci. Technol.* 1999, **33**, 1179−1184.

16. M. Zhu, P. Northrup, C. Shi, S. J. L. Billinge, D. L. Sparks, G. A. Waychunas, *Environ. Sci. Technol. Lett*. **2014**, 1, 97−101.

17. J. Antelo, F. Arce, S. Fiol, *Chemical Geology* 2015, **410**, 53–62.

18. B. J. Lafferty, R. H. Loeppert, Environ*. Sci. Technol.*, 2005, **39**, 2120–2127.

19. X. Gao, R. A. Root, J. Farrell, W. Ela, J. Chorover, *Applied Geochemistry* 2013, **38**, 110–120.

20. C. J. Goffinet, and S. E. Mason, *J. Environ. Monit.* 2012, **14**, 1860–1871.

21. M. Blanchard, M. Morin, M. Lazzeri, E. Balan, I. Dabo, *Geochimica et Cosmochimica Acta*, 2012, **86**, 182–195.

22. K. Otte, W. W. Schmahl, R. Pentcheva, *J. Phys. Chem. C* 2013, **117**, 15571−15582.

23. A. C. Q. Ladeira, V. S. T. Ciminelli, H. A. Duarte, M. C. M. Alves, A. Y. Ramos, *Geochim. Cosmochim. Acta* 2001, **65**, 1211.

24. Q. Shi, L. Yan, T. Chan, C. Jing, *ACS Appl. Mater. Interfaces* 2015, 7, 26735−26741.

25. S. E. Baltazar, A. H. Romero, M. Salgado, *Comput. Mater. Sci.* 2017, **127**, 110–120.

26. D. M. Sherman, S. R. Randall, *Geochimica et Cosmochimica Acta*, 2003, **67**, 4223–4230.

27. N. Y. Dzade, A. Roldan, N. H. de Leeuw, *Environ. Sci. Technol.*, 2017, **51**, 3461–3470.

28. M. Blanchard, K. Wright, J. D. Gale, C. R. A. Catlow, *J. Phys. Chem. C* 2007, **111**, 11390−11396.

29. G. Kresse and J. Furthmüller, *J. Comput. Mat. Sci.* 1996, ***6***, 15−50.

30. G. Kresse and J. Hafner, *J. Phys. Rev. B.* 1993, ***47***, 558.

31. P. E. Blöchl, *Phys. Rev. B.* 1994, ***50***, 17953.

32. J. P. Perdew, K. Burke, and M. Ernzerhof, Phys. Rev. Lett. 1996, **77**, 3865−3868.

33. V. I. Anisimov, F. Aryasetiawan, and A. I. Lichtenstein, *J. Phys.: Condens. Matter*. 1997, **9**, 767–808.

34. G. Rollmann, A. Rohrbach, P. Entel, J. Hafner *Phys. Rev. B*. 2004, **69**, 165107.

35. N. Y. Dzade, A. Roldan, N. H. de Leeuw, *Minerals* 2014, **4**, 89−115.

36. D. Santos-Carballal, A. Roldan, R. Grau-Crespo, N. H. de Leeuw, *Phys. Chem. Chem. Phys*. 2014, **16**, 21082-21097.

37. L. Wu, N. Y. Dzade, L. Gao, D. O. Scanlon, Z. Öztürk, N. Hollingsworth, B. M. Weckhuysen, E. J. M. Hensen, N. H. de Leeuw, J. P. Hofmann, *Adv. Mater.* 2016, **28**, 9602–9607.

38. S. Grimme, J. Antony, S. Ehrlich, and S. Krieg, *J. Chem. Phys*. 2010, 132, 154104.

39. H. J. Monkhorst, and J. D. Pack, *Phys. Rev. B.* 1976, **13**, 5188−5192.

40. F. M. Michel, L. Ehm, S. M. Antao, P. L. Lee, P. J. Chupas, G. Liu, D. R. Strongin, M. A. A. Schoonen, B. L. Phillips, and J. B. Parise, *Science,* 2007, **316**, 1726–1729.

41. R. Demichelis, Y. Noel, C. M. Zicovich-Wilson, C. Roetti, L. Valenzano, R. Dovesi, *J. Phys.: Conf. Ser*. 2008, **117**, 012013.

42. M. Ji, J. Cai, Y. Ma, and L. Qi, *ACS Appl. Mater. Interfaces* 2016, 8, 3651−3660.

43. G. W. Watson, E. T. Kelsey, N. H. de Leeuw, D. J. Harris and S. C. Parker, *J. Chem. Soc., Faraday Trans*., 1996, 92, 433.

44. P. W. Tasker, *J. Phys. C: Solid State Phys*., 1979, 12, 4977.

45. G. Makov and M. C. Payne, *Phys. Rev. B.* 1995, 51, 4014

46. S. Baroni, S. de Gironcoli, A. Dal Corso, P. Giannozzi, *Rev. Mod. Phys.* 2001, **73**, 515–562.

47. N. Pinney, J. D. Kubicki, D. S. Middlemiss, C. P. Grey, D. Morgan, *Chem. Mater*. 2009, **21**, 5727–5742.

48. A. Manceau, *Clay Minerals* 2009, **44**, 19–34.

49. F. M. Michela, V. Barrónc, J. Torrent, M. P. Morales, C. J. Serna, J-F Boily, Q. Liu, A. Ambrosini, A. C. Cismasu, and G. E. Brown Jr., *PNAS*, 2010, **107**, 2787–2792.

50. G. He, M. Zhang, G. Pan, *J. Phys. Chem. C* 2009, **113**, 21679–21686.

51. N. Y. Acelas, S. M. Mejia, F. Mondragón, E. Flórez, *Comp. Theor. Chem.* 2013, **1005**, 16–24.

52. A. Manceau, *Geochim. Cosmochim. Acta* 1995, **59**, 3647–3653.

53. S. Fendorf, M. J. Eick, P. Grossl, D. L. Sparks, *Environ. Sci. Technol.* 1997, **31**, 315–320.

54. W. C. Lee, S. O. Kim, J. Ranville, S. T. Yun, S. H. Choi, *Environ Earth Sci.* 2014, **71**, 3307–3318.

55. T. M. Loehr, R. A. Plane, *Inorg. Chem*. 1968, 7, 1708−1714.

56. K. Müller, V. S. T. Ciminelli, M. S. S. Dantas, S. Willscher, *Water Res.* 2010, **44**, 5660–5672.

57. T. Shimanouchi, *J. Phys. Chem.* 1977, **6**, 3.

List of Tables

Table 1: Lattice constants, selected bond lengths, and Fe magnetic moment for ferrihydrite.

	Theory (GGA+U = 4 eV)		Experiment Michel *et al.*[40]	
Property	This work	Other work[47]	6-line-Fh	2-line-Fh
$a = b$ (Å)	5.955	5.97	5.928	5.958
c (Å)	9.222	9.37	9.126	8.965
$Fe1_{oct}$–O (Å)	1.968(x 2), 2.059(x 2), 2.029, 2.066	1.981(x 2), 2.075(x 2), 2.040, 2.068	1.933, 2.012(x 2), 2.140(x 2), 2.042	1.918, 1.979(x 2), 2.036(x 2), 2.052
$Fe2_{oct}$–O (Å)	1.942(x 3), 2.183(x 3)	1.952(x 3), 2.206(x 3)	1.874(x 3), 1.964(x 3)	1.883(3), 2.082(3)
$Fe3_{tet}$–O (Å)	1.903(x 1), 1. 913(x 3)	1.916(x 1) 1.923(x 3)	1.790(x 1) 1.953(x 3)	1.959(x 1) 2.019(x 3)
O–H (Å)	0.985	1.000	–––	–––
$m_s(Fe1_{oct})$ (μB)	4.20	4.00	–––	–––
$m_s(Fe2_{oct})$ (μB)	4.17	–––	–––	–––
$m_s(Fe3_{tet})$ (μB)	4.13	–––	–––	–––

Table 2: Adsorption energies (eV) and optimized geometries (Å) of H_3AsO_3 adsorption configurations on Fh(110) surface at intermediate (-OH/-H_2O) and high (-OH) pH conditions, (deprot. = deprotonated).

Surface state	Configuration	E_{ads}	d(As–O1)	d(As–O2)	d(As–O3)	d(O_{mol}–Fe)	d(As–Fe)	d(As–O_{surf})
Fh(110)−OH/−H_2O	MM(Fe−O)	–1.25	1.878	1.850	1.826	2.101	3.185	2.389
	BB(Fe−O)	–2.53	1.926	1.786	$1.752_{deprot.}$	1.982/2.154	3.606	3.502
	solv-MM(Fe−O)	–2.49	1.863	1.826	$1.777_{deprot.}$	1.965	3.616	2.879
	solv-BB(Fe−O)	–3.60	1.957	$1.777_{deprot.}$	$1.752_{deprot.}$	1.957/2.097	3.573	3.459
	Outer-sphere	–1.98						
Fh(110)−OH	solv-MM(Fe−O)	–2.23	1.826	1.887	$1.763_{deprot.}$	2.147	3.692	3.527
	solv-BB(Fe−O)	–3.39	1.756	1.831	1.914	2.141/2.302	3.222	2.682
	Outer-sphere	–1.83	1.803	1.803	1.852	---	---	---

Table 3: Adsorption energies (eV) and optimized geometries (Å) of As(V) adsorption configurations on Fh(110) surface at intermediate (-OH/-H_2O) and high (-OH) pH conditions, (deprot. = deprotonated).

Species (Surf state)	Configuration	E_{ads}	*d*(As–O1)	*d*(As–O2)	*d*(As–O3)	*d*(As–O4)	*d*(O_{mol}–Fe)	*d*(As–Fe)	*d*(As–O_{surf})
H_3AsO_4 (−OH/−H_2O)	MM(Fe−O)	–1.34	1.818	1.769	1.743	1.641	2.147	3.402	3.580
	BB(Fe−O)	–2.85	1.765	1.751	1.704	$1.702_{deprot.}$	2.010/ 2.077	3.496	2.921
	solv-MM(Fe−O)	–2.84	1.774	1.756	1.707	$1.687_{deprot.}$	1.987	3.268	3.349
	solv-BB(Fe−O)	–4.18	1.757	1.740	1.709	$1.704_{deprot.}$	1.965, 2.003	3.312	2.257
	Outer-sphere	–2.13	1.764	1.796	1.769	1.640	---	---	---
$H_2AsO_4^-$ (−OH/−H_2O)	solv-MM(Fe−O)	–2.75	1.774	1.756	1.707	$1.687_{deprot.}$	1.987	3.268	3.349
	solv-BB(Fe−O)	–3.97	1.757	1.740	1.709	$1.704_{deprot.}$	1.965, 2.003	3.312	2.257
	Outer-sphere	–1.98	1.764	1.796	1.769	1.640	---	---	---
H_3AsO_4 (−OH)	solv-MM(Fe−O)-1	–2.87	1.735	1.748	1.762	$1.678_{deprot.}$	1.969	3.289	4.063
	solv-MM(Fe−O)-2	–2.54	1.730	1.745	1.769	1.683	2.051	3.169	3.217
	Outer-sphere	–2.08	1.776	1.755	1.744	1.658	---	---	---

Table 4: Molecular vibrational frequencies (in cm^{-1}) of adsorbed H_3AsO_3 and H_3AsO_4 on Fh(110) surface with mixed -OH/-H_2O composition.

		ν(As−O)				ν(O−H)		
As species	Configuration	As−O_H	As−O_H	As−O_H	As−O	O1−H	O2−H	O3−H
H_3AsO_3	MM(Fe−O)	622	570	526	−−−	3714	3699	2066
	BB(Fe−O)	$772_{deprotonated}$	683	492	−−−	3678	$2855_{deprotonated}$	2371
	MM(Fe−O)-solvated	$725_{deprotonated}$	616	559	−−−	3602	3052	$2873_{deprotonated}$
	BB(Fe−O)-solvated	$771_{deprotonated}$	$665_{deprotonated}$	448	−−−	3027	$2642_{deprotonated}$	$2156_{deprotonated}$
H_3AsO_4	MM(Fe−O)	709	678	634	938	3708	3596	3468
	BB(Fe−O)	$855_{deprotonated}$	731	696	809	3713	$3010_{deprotonated}$	2579
	MM(Fe−O)-solvated	$870_{deprotonated}$	707	672	798	3279	$3242_{deprotonated}$	2237
	BB(Fe−O)-solvated	$814_{deprotonated}$	757	715	807	$2326_{deprotonated}$	2304	2223

List of Figures

Figure 1: (a) Structure of ferrihydrite in terms of FeO_6 octahedra and (b) ferrimagnetic spin ordering indicated by up (blue) and down (yellow) arrows at the Fe sites. (Atomic colour scheme: Fe = grey, O = red, and H = white).

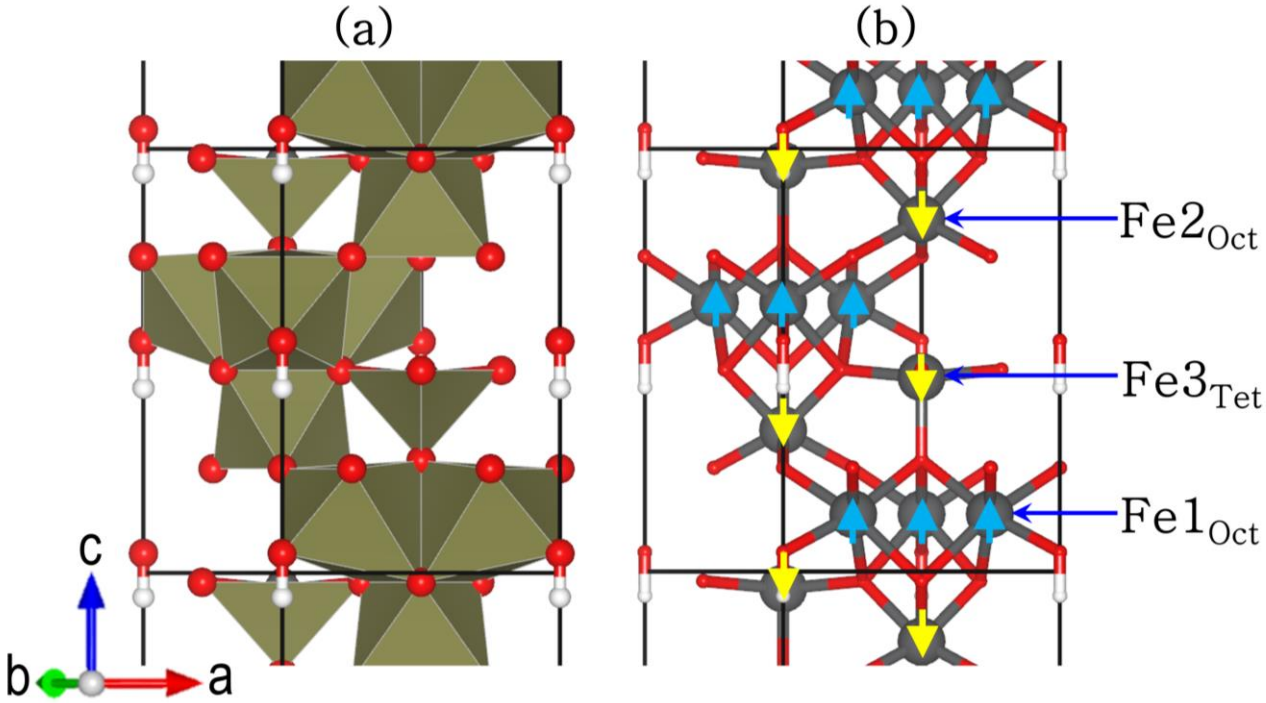

Figure 2: Geometry-optimized structures of Fh(110) surface covered with -OH/-H_2O mixtures in side (a) and top (b) views. (Atomic colour scheme: Fe_{Oct} = grey, Fe_{Tet} =blue, O = red, and H = white).

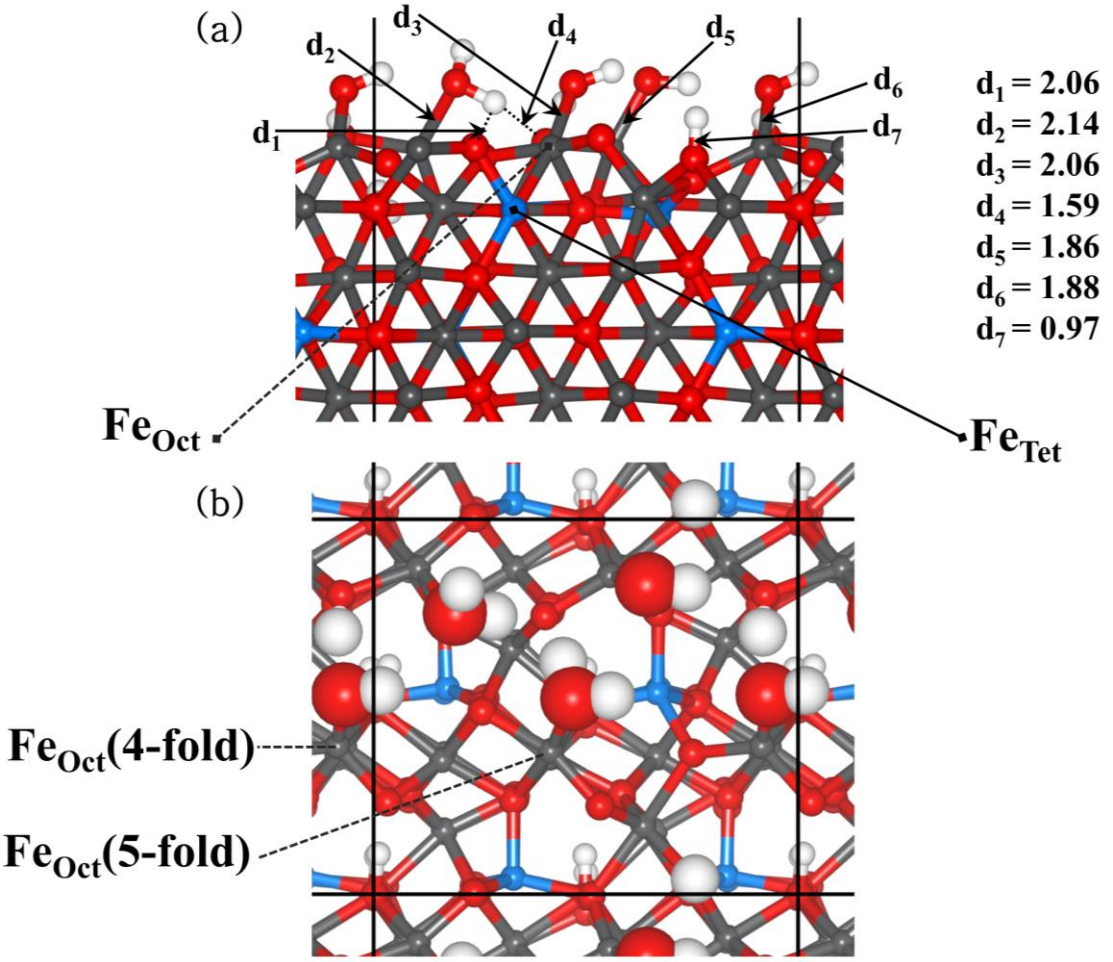

Figure 3: Geometry-optimized structures of Fh(110) surface covered with only -OH in side (a) and top (b) views. (Atomic colour scheme: Fe_{Oct} = grey, Fe_{Tet} =blue, O = red, and H = white).

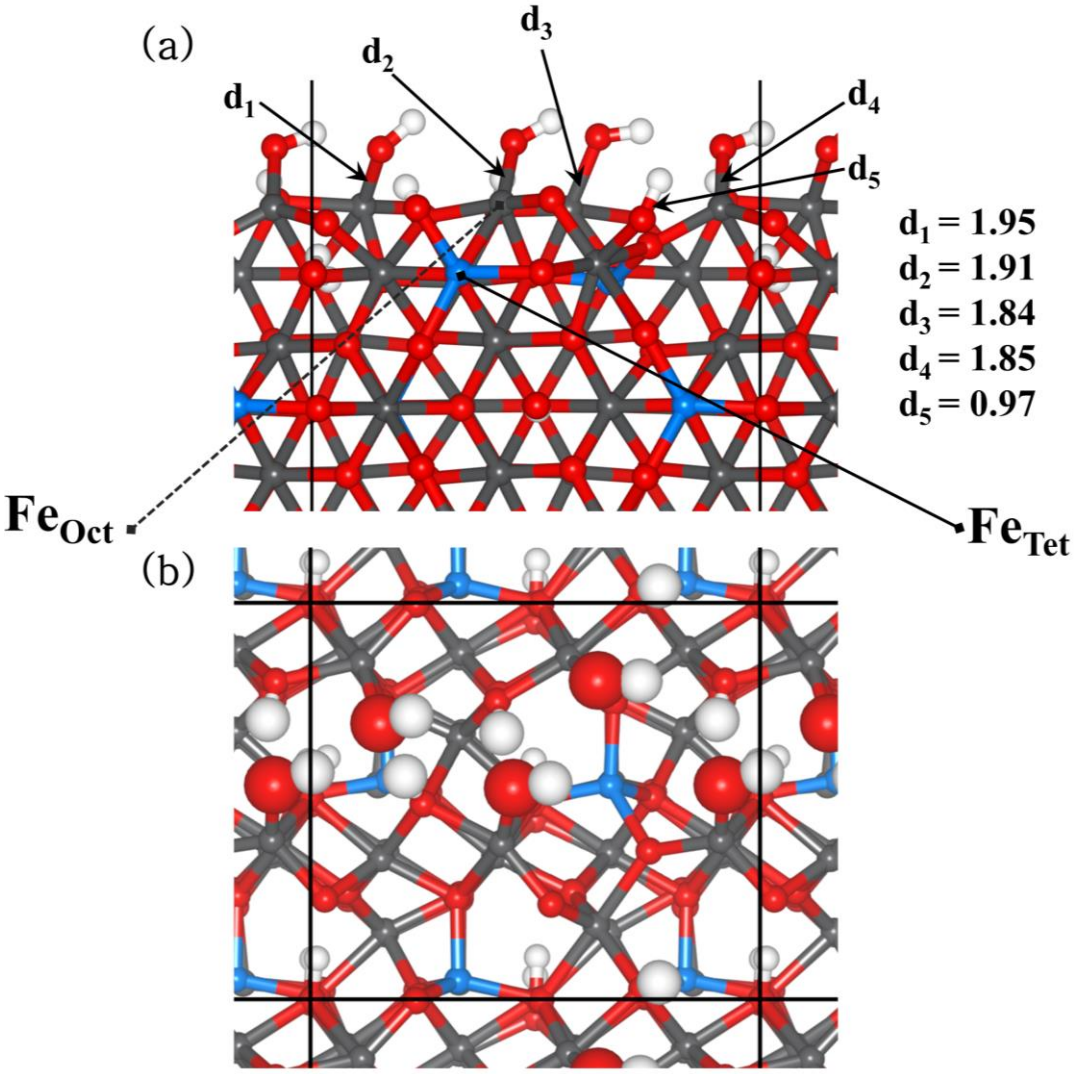

Figure 4: Schematic diagram of surface protonation-deprotonation processes controlled by pH conditions.

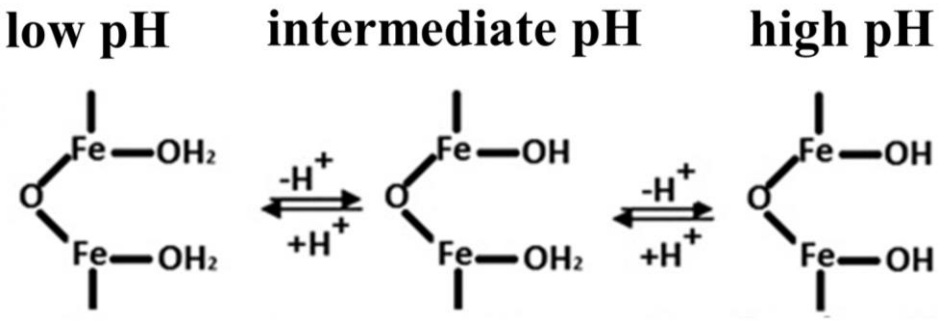

Figure 5: Optimized structures of inner and outer sphere adsorption complexes of H_3AsO_3 on Fh(110) surface covered with mixed –OH/–H_2O. Top (a & b) and bottom (c, d, & e) panels denote non-solvated and solvated complexes, respectively (atomic colour scheme: Fe = grey, O_{surf} = red, O_{mol} = light slate blue, As = green, and H = white). Bond distances are in Angstrom unit.

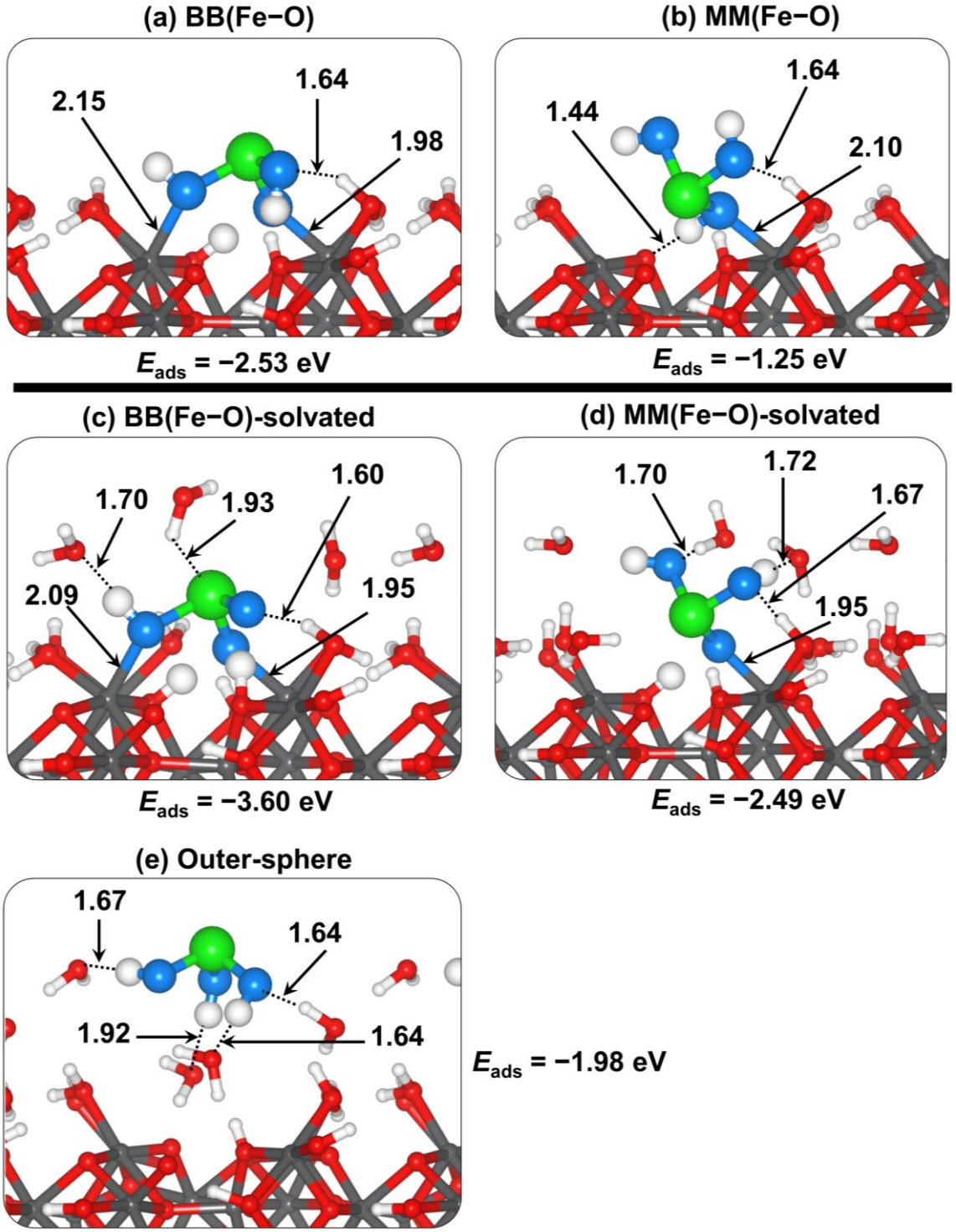

Figure 6: Optimized structures of inner and outer sphere adsorption complexes of H_3AsO_3 on Fh(110) surface covered with -OH. (Atomic colour scheme: Fe = grey, O_{surf} = red, O_{mol} = light slate blue, As = green, and H = white). Bond distances are in Angstrom unit.

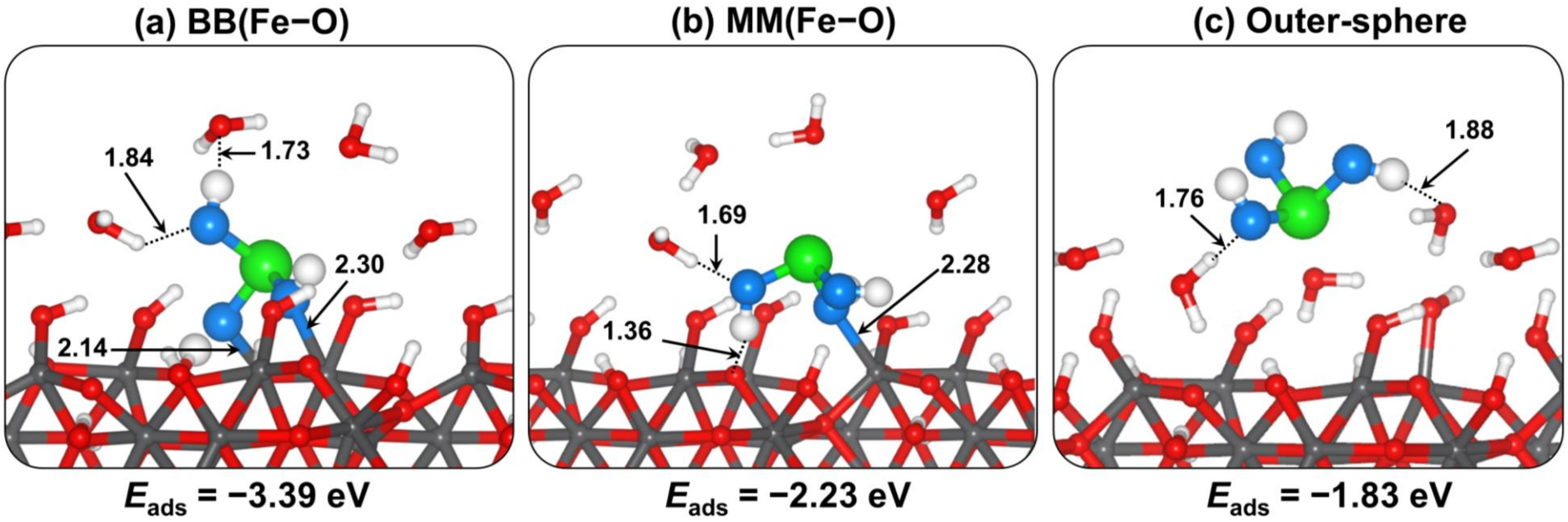

Figure 7: Optimized structures of inner and outer sphere adsorption complexes of H_3AsO_4 on Fh(110) surface covered with mixed –OH/–H_2O. Top (a & b) and bottom (c, d, & e) panels denote non-solvated and solvated complexes, respectively (atomic colour scheme: Fe = grey, O_{surf} = red, O_{mol} = light slate blue, As = green, and H = white). Bond distances are in Angstrom unit.

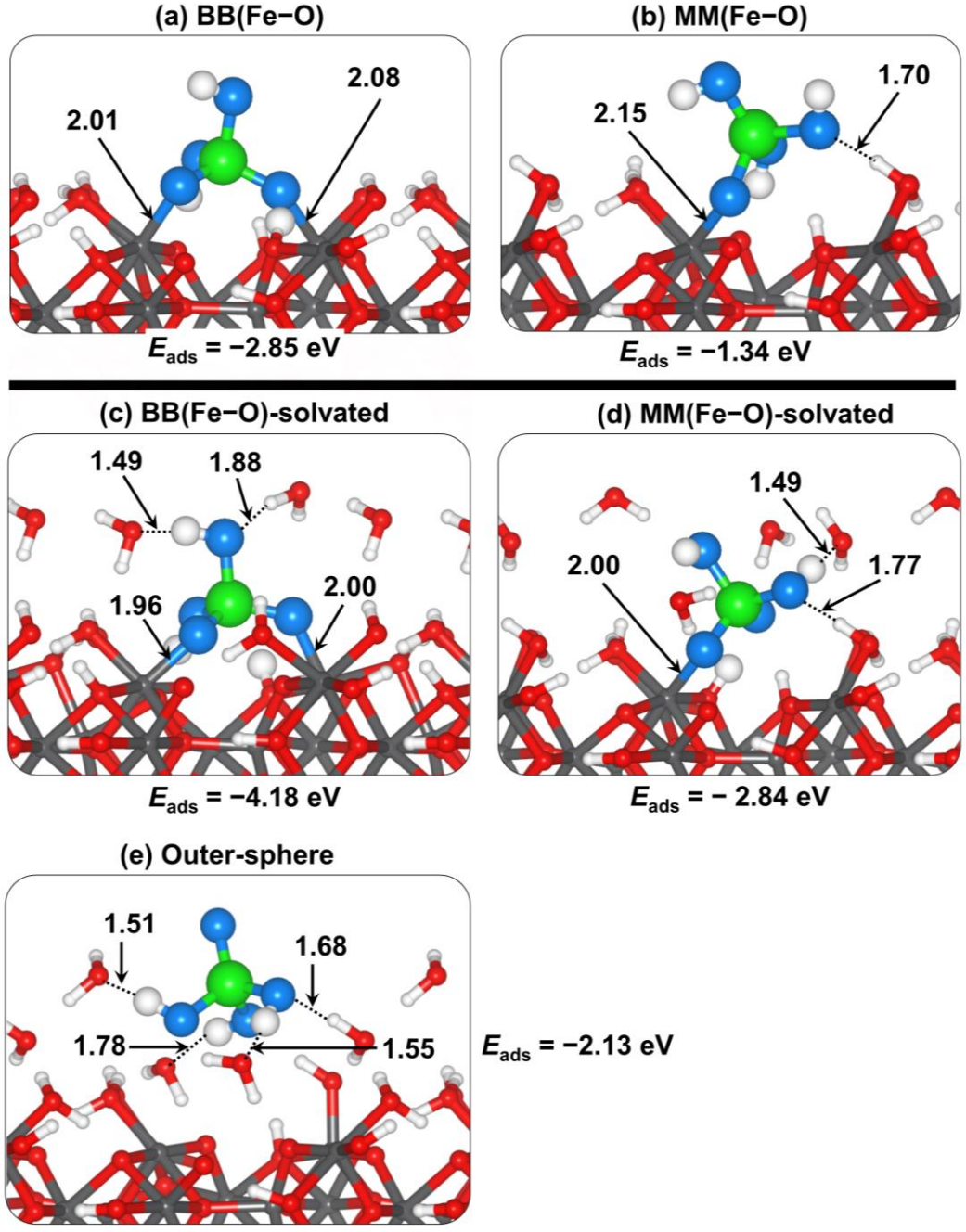

Figure 8: Optimized structures of inner and outer sphere adsorption complexes of H_3AsO_4 on Fh(110) surface covered with mixed -OH. (Atomic colour scheme: Fe = grey, O_{surf} = red, O_{mol} = light slate blue, As = green, and H = white). Bond distances are in Angstrom unit.